


Robust experimental data assimilation for the Spalart-Allmaras turbulence model

Deepinder Jot Singh Aulakh ^{*,†}

*Department of Mechanical and Materials Engineering, [Queen's University](#),
130, Stuart Street, Kingston, Ontario, Canada K7L 2V9*

Xiang Yang

*Department of Mechanical Engineering, [Pennsylvania State University](#), E327 Westgate,
University Park, Pennsylvania 16801, USA*

Romit Maulik 

*Information Sciences and Technology, [Pennsylvania State University](#), E327 Westgate,
University Park, Pennsylvania 16801, USA*



(Received 10 March 2024; accepted 23 July 2024; published 22 August 2024)

This study presents a methodology focusing on the use of computational model and experimental data fusion to improve the Spalart-Allmaras (SA) closure model for Reynolds-averaged Navier-Stokes solutions. In particular, our goal is to develop a technique that not only assimilates sparse experimental data to improve turbulence model performance, but also preserves generalization for unseen cases by recovering classical SA behavior. We achieve our goals using data assimilation, namely the ensemble Kalman filtering approach, to calibrate the coefficients of the SA model for separated flows. A holistic calibration strategy is implemented via the parametrization of the production, diffusion, and destruction terms. This calibration relies on the assimilation of experimental data collected in the form of velocity profiles, skin friction, and pressure coefficients. Despite using observational data from a single flow condition around a backward-facing step (BFS), the recalibrated SA model demonstrates generalization to other separated flows, including cases such as the two-dimensional (2D) NASA wall mounted hump and the modified BFS. Significant improvement is observed in the quantities of interest, i.e., the skin friction coefficient (C_f) and the pressure coefficient (C_p), for each flow tested. Finally, it is also demonstrated that the newly proposed model recovers SA proficiency for flows, such as a NACA-0012 airfoil and axisymmetric jet, and that the individually calibrated terms in the SA model target specific flow-physics wherein the calibrated production term improves the recirculation zone while destruction improves the recovery zone.

DOI: [10.1103/PhysRevFluids.9.084608](https://doi.org/10.1103/PhysRevFluids.9.084608)

I. INTRODUCTION

Reynolds-averaged Navier-Stokes (RANS) -based simulations are employed extensively for the analysis of turbulent flows, primarily due to their ability to provide swift engineering insights due to

^{*}Contact author: 16djsa@queensu.ca

[†]Also at Argonne Leadership Computing Facility, 240, Argonne National Laboratory, Lemont, IL 60439, USA.

shorter turnover durations. RANS equations consist of time-averaged descriptions of the classical Navier-Stokes equations, and they are used for the predictive modeling of steady-state characteristics of turbulent flows. Within the RANS framework, instantaneous quantities are decomposed using the Reynolds decomposition into components representing time-averaged and fluctuating aspects. However, the presence of Reynolds stresses, which result from unclosed fluctuation terms, necessitates additional model specifications to achieve RANS closure. One notable closure model utilized extensively in aerospace applications is the Spalart-Allmaras (SA) model [1]. Despite its popularity, RANS solutions (using various closure models, including SA) are susceptible to inaccurate predictions in flow regimes involving separation and adverse pressure gradients. These errors stem primarily from the assumptions inherent in RANS models, which are valid for a limited range of flow scenarios.

Despite increased computational power, the utilization of high-fidelity simulations, such as direct numerical simulation (DNS) and large-eddy simulation (LES), remains constrained when addressing real-world problems [2,3]. As a result, enhancing the accuracy of Reynolds-averaged Navier-Stokes (RANS) models continues to be an active area of research [4,5]. Recently, there has been a surge in the application of machine learning (ML) and data-driven techniques to enhance closure models [6]. The majority of investigations in this field concentrate on either substituting or enhancing the closure model using ML approaches [7–11]. A recently popular method involves substituting the closure model with a trained ML model. In this context, a trained ML model, derived from either high-fidelity DNS data or RANS simulations, replaces the solution variables [7,12–14]. While a model trained exclusively on RANS solutions might not lead to accuracy improvements, it holds implications for improving the convergence of the RANS solver, as observed by Maulik *et al.* [15] and Liu *et al.* [16]. Using DNS data, Ling *et al.* [17] introduced the tensor basis neural network (TBNN) to enhance the accuracy of the RANS solver. This approach employed high-fidelity DNS data to train the neural network (NN), utilizing a tensor combination technique originally proposed by Pope [18]. Notably, TBNNs inherently uphold Galilean invariance and possess adaptability for capturing nonlinear relationships, thus adhering to some of the foundational principles proposed by Spalart *et al.* [19]. Additionally, Wang *et al.* [20] introduced an ML model, aiming to learn the disparities between RANS and DNS data. To further enhance the convergence and stability of the RANS-ML model, techniques involving the decomposition of Reynolds stresses in linear and nonlinear terms [21,22] and the imposition of non-negative constraints were incorporated on linear terms [23].

In the other approach, i.e., augmenting the closure models, a prominent approach involves the calibration of existing closure models by experimental or DNS data [24–27]. Ray *et al.* [9,28], focused on calibrating three coefficients—namely, C_μ , $C_{\epsilon 1}$, and $C_{\epsilon 2}$ —within the k - ϵ model. Calibration was carried out using experimental data for the interaction of a compressible jet with a cross-flow. Notably, the outcomes of the calibrated RANS model demonstrated significantly closer alignment with experimental data in comparison to those obtained using nominal constants.

Additionally, the concept of field inversion has been explored extensively for the refinement of closure models [29–32]. Duraisamy *et al.* [33] and Chongyang *et al.* [34] introduced modifications to the production term within the transport equation by incorporating a spatially variable factor. This approach was complemented by the incorporation of flow features as input for the ML model, thereby enhancing the generalizability of the modified model.

Bin *et al.* [35] proposed the concept of progressive machine learning, arguing that machine-learned augmentations must not negatively impact the existing calibrations. Following this line of thinking, Bin *et al.* [36] calibrated the SA turbulence model using experimental and DNS data. Their work aimed to achieve a more universally applicable improvement for various flow conditions. It involved replacing the SA model's coefficients with NNs trained through Bayesian optimization. Particularly noteworthy was the finding that the most significant enhancements were attributed to the destruction term within the model. Subsequently, Bin *et al.* [37] extended their study to two-equation RANS closures, where they further identified the importance of preserving the law of wall,

which is likely to be disrupted with unconstrained calibration of ML-based models. This disruption could affect the behavior of the calibrated model for cases outside the training data set.

Recently, another data-driven method, namely data assimilation using ensemble Kalman filtering (EnKF) [38–40], has been explored for improving RANS closures. Zhang *et al.* [38] employed the EnKF technique to train TBNN originally introduced by Ling *et al.* [17]. The application of EnKF for TBNN training exhibited a performance akin to the original study. However, a noteworthy advantage emerged: the capacity to employ sparse and noisy data to effectively train TBNNs. Moreover, EnKF was effectively employed in an online manner, facilitating real-time training of TBNNs using indirect measurements.

Kato *et al.* [40] used EnKF to integrate experiments with computational fluid dynamics (CFD). Surface pressure data from experiments were used to improve the accuracy of the simulations. Yang and Xiao [32] utilized a regularized EnKF approach to enhance the transition model. Experimental data were used to calibrate transition location within the model, leading to notable improvements. Kato and Obayashi [27] used simulation data from flow over a flat plate to estimate the parameters of the SA model. The EnKF approach applied in this case resulted in parameters whose accuracy was consistent with that of the original parameters. Additionally, Kato *et al.* [26] used EnKF to improve the modified Menter $k\text{-}\omega$ model. In contrast with the aforementioned studies, in our approach we perform an optimization of a single parameter (a), which results in improved accuracy for flows with separation and adverse pressure gradients.

Our research revisits the calibration of the SA turbulence model while utilizing sparse and noisy experimental data. To achieve this, EnKF is employed to calibrate the coefficients of the SA model. Furthermore, the current study comprehensively employs calibration, encompassing all elements such as production, diffusion, and destruction terms. The calibration process is framed as an inverse problem, wherein iterative corrections of the SA coefficients are performed within an EnKF-based loop. The focus of this work is to harness sparse and noisy experimental data for the calibration of the SA model in scenarios involving separated flows. Specifically, the coefficients are calibrated using the backward-facing step (henceforth denoted BFS1) configuration [41], while the subsequent testing encompasses the two-dimensional NASA wall mounted hump (2D-WMH) case [42] and a modified backward-facing step (denoted BFS2) scenario with altered step height [36,43]. To determine that the calibrated model is not detrimental to attached and unbounded flows, tests were also done for flow around an airfoil and a zero pressure gradient boundary layer.

II. BACKGROUND

The SA model was proposed by Spalart *et al.* [1], and it remains a workhorse for aerospace design using RANS. The model takes into account the convection, diffusion, production, and destruction of the eddy viscosity ($\nu_t = f_{v1} \tilde{\nu}$) in a single transport equation as follows:

$$\frac{D\tilde{\nu}}{Dt} = \underbrace{C_{b1}\tilde{S}\tilde{\nu}}_{\text{Production}} - \underbrace{C_{w1}f_w\left(\frac{\tilde{\nu}}{d}\right)^2}_{\text{Destruction}} + \underbrace{\frac{1}{\sigma}\{\nabla \cdot [(v + \tilde{\nu})\nabla \tilde{\nu}] + C_{b2}|\nabla \tilde{\nu}|^2\}}_{\text{Diffusion}}, \quad (1)$$

where the coefficients C_{b1} , σ , and C_{b2} take the values 0.1355, 0.666, and 0.622, respectively. C_{w1} and f_w are given by Eqs. (2) and (3), respectively, as follows:

$$C_{w1} = \frac{C_{b1}}{\kappa^2} + \frac{1 + C_{b2}}{\sigma}, \quad (2)$$

where $\kappa = 0.41$ is a von Karman constant,

$$f_w = g\left(\frac{1 + C_{w3}^6}{g^6 + C_{w3}^6}\right), \quad g = r + C_{w2}(r^6 - r), \quad (3)$$

where $C_{w3} = 2$ and $C_{w2} = 0.3$. \tilde{S} is the modified strain rate (S) of the mean velocity field:

$$\tilde{S} = S + \tilde{\nu} \frac{f_{v2}}{\kappa^2 d^2}, \quad (4)$$

where d is the distance from the nearest wall, and f_{v2} is dependent on $\chi = \tilde{\nu}/\nu$, $C_{v1} = 7.1$, and f_{v1} as follows:

$$f_{v2} = 1 - \frac{\chi}{1 + \chi f_{v1}}, \quad f_{v1} = \frac{\chi^3}{C_{v1}^3 + \chi^3}. \quad (5)$$

The SA model provides high accuracy for equilibrium flows, but it fails to accurately capture separation and recovery in nonequilibrium wall-bounded separating flows. Our study aims to address this drawback by using a data-assimilation-based calibration of the SA model for separating flows. Moreover, we use sparse experimental data to enable this calibration. The constraints for the calibration in this study are summarized as follows:

- (i) Our methodology must utilize noisy and sparse experimental data for calibration.
- (ii) Our calibrated model must generalize, i.e., the data from one type of separating flow at a single Reynolds number (Re), the boundary condition, and the geometry should be enough to improve the accuracy of the model in other separating flows.
- (iii) The calibration should not distort the model's original behavior in equilibrium flows.

III. METHODOLOGY

A. Ensemble Kalman Filtering for calibration

Ensemble Kalman filtering (EnKF) is commonly used in data assimilation to aid in the estimation of system states, such as velocity and pressure in a flow field, given sparse observational data [38]. In the current study, we use EnKF for calibrating the SA model. Before going into further details about calibration, we first introduce the observation matrix (H) free implementation of EnKF used in the current study [44]:

$$X^p = X + \frac{1}{N-1} A(HA)^T P^{-1} (D - HX), \quad (6a)$$

where

$$P = \frac{1}{N-1} (HA)(HA)^T + R, \quad (6b)$$

$$A = X - E(X), \quad HA = HX - E(HX). \quad (6c)$$

Here, matrix X is denoted as the prior ensemble, and X^p represents the posterior ensemble. Both matrices have dimensions $n \times N$. The value n pertains to the number of coefficients selected for calibration from Eq. (1), and N refers to the number of members in the ensemble. To exemplify, if we consider the instance of selecting C_{b1} , C_{b2} , and σ , then n would be equal to 3. D is an $m \times N$ matrix containing experimental data, where m signifies the number of probe points. Additionally, R represents the covariance matrix of random noise in D . The central objective revolves around employing the coefficients derived from the SA model as elements of matrix X while utilizing the data matrix D to refine and calibrate these coefficients. The outcome is the matrix X^p , which encapsulates the calibrated coefficients. This process aligns with the broader aspiration of refining understanding and enhancing the accuracy of the SA model through the integration of both theoretical insights and empirical observations. Notably, for covariance reduction, an identity matrix is added to Eq. (6b). This covariance reduction considerably reduces the required N , hence reducing the computation cost. The tradeoff here is an increase in the stochastic nature of the optimization. This was deemed acceptable for the current application.

The selection of HX is contingent on the available experimental data. For instance, if experimental data for velocity are available, the HX will be the velocity obtained after solving the RANS

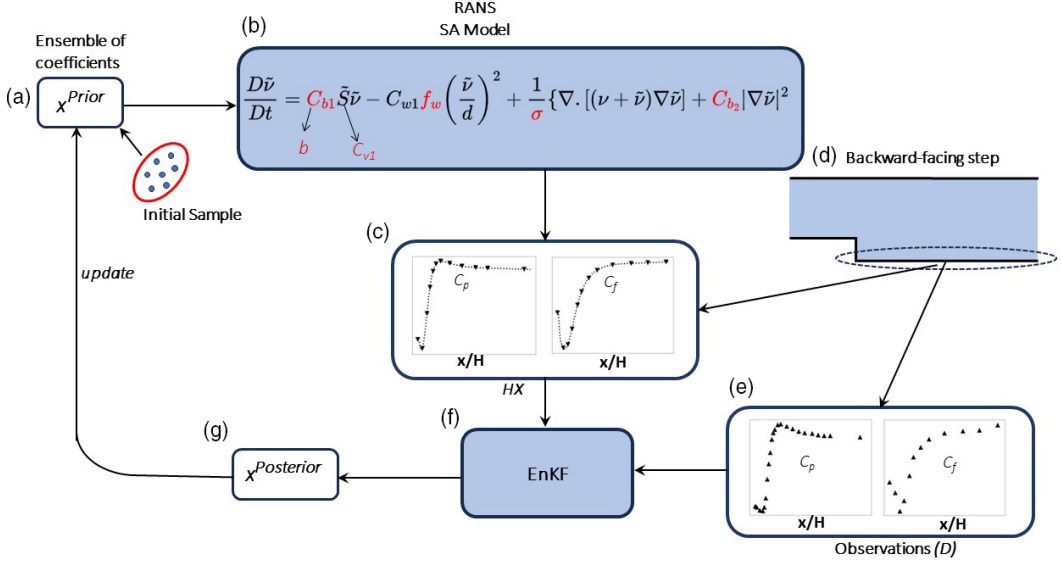


FIG. 1. EnKF calibration loop. (a) An ensemble (X) of the SA coefficients—for the first iteration, X is sampled from an initial distribution determined by a parametric analysis in Appendix A. (b) The RANS solver and the SA model calculate the flow variables based on the SA coefficients in X , the coefficients used in the ensemble are highlighted in red, and the coefficient b is defined later. (c) The extracted quantities of interest (QOIs) from OpenFOAM at specified locations serve as the HX for the EnKF. (d) The QOIs in the current study are C_f and C_p along the bottom wall. (e) $D_{m \times N}$ matrix for the available data for the QOIs. m is the number of probe points, and N is the ensemble size picked from the Gaussian distribution. (g) Updated X^p based on the EnKF in (f).

equations by using X as the SA coefficients. It should be noted that the HX will be formulated by only extracting the locations where the experimental data are available. This is illustrated in Fig. 1(c), where the values are extracted along the lower wall of the BFS.

B. Calibration loop

The iterative EnKF calibration loop used in the current study is outlined as follows:

(i) Sample SA coefficients X based on an initial prior distribution [Fig. 1(a)]. The initial distribution's upper and lower bounds are determined after undertaking a parametric analysis (Appendix A) of the SA model for a flow over the BFS case.

(ii) The X , i.e., the sampled coefficients, are used to obtain evaluations for HX . The observation matrix H encompasses a RANS simulation and the extraction of the quantity of interest (QOI) at a given location in the domain [Figs. 1(b) and 1(c)]. The locations are dictated by the available experimental data for the QOIs. In the current case, the QOIs are the friction (C_f) and pressure (C_p) coefficients, available at the lower wall downstream of the step in BFS flow [Fig. 1(d)].

(iii) The HX is further substituted into Eq. (6a) to obtain posterior ensemble X^p . The X^p serves as an ensemble distribution for the next iteration.

EnKF possesses desirable attributes such as the ability to accommodate noisy data, quantification of uncertainty, and enabling gradient-free optimization. Notably, the gradient-free optimization not only streamlines the EnKF's implementation process, but it also endows it with heightened adaptability for integration with diverse computational fluid dynamics solvers, thereby reducing the necessity for intrusive modifications of its source code. In addition, the HX can be easily modified to use any QOI for which the calibration data are available. This customization process

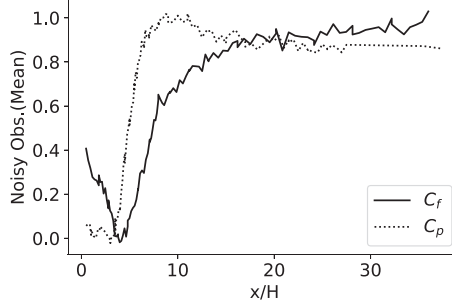


FIG. 2. Mean of the calibration data D used for the current study. The values of C_f and C_p are plotted along the bottom wall of the BFS. The baseline data were obtained from the NASA turbulence repository [45], and a noise $\epsilon \sim \mathcal{N}(0, \sigma_D = 0.05)$ is added to formulate the D matrix.

requires the (usually straightforward) extraction of the requisite QOI directly from the solution field. Moreover, the EnKF's proficiency in effectively managing noisy data aligns well with experimental data that have inherent measurement variabilities. This particular attribute underscores the EnKF's suitability for assimilating real-world experimental observations into the calibration process, thereby enhancing its efficacy in bridging theoretical models with empirical data.

C. Calibration data (D)

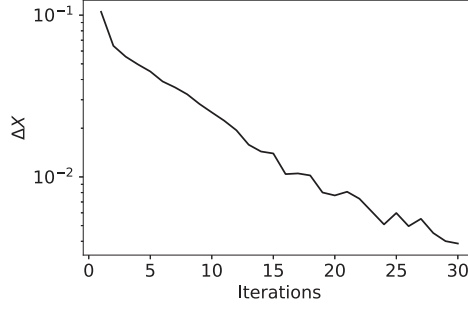
We begin this section by noting that the data-driven calibration proposed in this research relied solely on experimental data. This is in contrast to similar studies that relied on DNS data for improving RANS models [36]. The requirement of only using experimental data presented challenges since the available data covered only a limited portion of the domain compared to DNS. This aligns with common data acquisition practices, as data are typically gathered predominantly along the walls, making them sparse, and there is naturally some level of noise in the readings. Consequently, the calibration process proposed necessitated a robust handling of sparsity and noise inherent in the experimental data.

The experimental data for the current study are from Driver and Seegmiller [41] and are retrieved from the NASA turbulence repository [41,45]. The data consist of C_f and C_p measurements along the bottom wall of the BFS downstream of the step. The data were interpolated to 112 locations along the bottom of the wall, i.e., $m = 112$. Notably, the magnitude of C_p is approximately three orders of magnitude higher than that of C_f . This difference in magnitude can cause the calibration to be weighted more towards C_p . Hence, the values of both C_p and C_f are separately scaled between (0, 1). Furthermore, a normally distributed noise $\epsilon \sim \mathcal{N}(0, \sigma_D = 0.05)$ is added to the experimental data, and $N = 5$ data vectors are sampled to formulate our D matrix. Figure 2 shows the mean value of observations.

D. Ensemble matrix (X)

To reiterate, the X matrix for this study is formulated by coefficients of the SA model. A parametric analysis outlined in Appendix A was performed to select the SA coefficients for calibration, in which C_{b1} , C_{w2} , C_{w3} , σ , and C_{v1} were selected. The parametric space for ensemble members is $C_{w2} \in [0.75, 1.75]$, $C_{w3} \in [1, 2]$, $\sigma \in [0.3, 2]$, and $C_{v1} \in [6, 9]$. In the original SA, C_{b1} has a value of 0.1355 for the entire domain. However, after an initial study (Appendix B) it was found that implementing a varying C_{b1} yields more flexibility in the model and may aid in improved calibration. Hence, the C_{b1} is further parametrized in terms of nondimensional field r as follows:

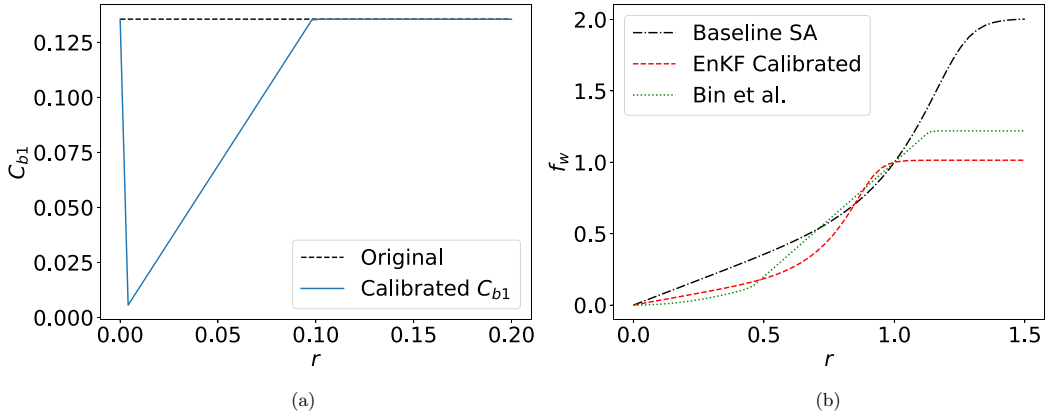
$$C_{b1} = \min(\max(r * b, c * r + d), 0.1355), \quad (7)$$


 FIG. 3. ΔX vs iterations for the calibration loop.

where $r \equiv v_t / Sk^2 d^2$, 0.1355 is the original value of C_{b1} . The parameter $b \in [1.5, 2.5]$ is also added to the ensemble matrix of the EnKF. To summarize, there are a total of five parameters that are calibrated using EnKF in this study. It is important to highlight that the initial decision involved parametrizing C_{b1} as $\min(r * b, 0.1355)$. While this parametrization yielded enhanced accuracy in the targeted flows of interest, it had the drawback of disabling the SA model when $r \approx 0$ for free shear flows. Consequently, the parametrization was modified for the inclusion of $c * r + d$ in Eq. (7) [Fig. 4(a)] to ensure the retention of C_{b1} values for $r \approx 0$, thereby preserving the model's applicability in free shear flows. Additionally, to mitigate the expansion of the parameter space for EnKF calibration, a decision was made to fix the values of c and d at -50 and 0.2 , respectively. These fixed scalars effectively maintain the SA model's behavior by linearly increasing the C_{b1} near $r \approx 0$ while yielding comparable behavior for the targeted flows as achieved by $\min(r * b, 0.1355)$. It should be noted that Eq. (7) was used for calibration.

E. Calibration metrics

The X matrix is calibrated in an iterative manner as discussed in Sec. III B. The performance of the calibration is monitored using the change in X in each iteration, specifically, as $\Delta X^i = \text{mean}(|X^i - X^{i-1}|)$ for the i th iteration. The EnKF loop is run for 30 iterations. Figure 3 shows ΔX versus iterations. The $\Delta X^{30} = 0.0038$ at the end of the EnKF deployment is considered acceptable for convergence. This is also evident from Appendix A, where such small changes in X do not result in any variation of the QOI.


 FIG. 4. (a) C_{b1} , (b) f_w vs r obtained from the calibrated coefficients. The original values are also plotted in corresponding plots. For additional comparison, the f_w obtained by Bin *et al.* [36] is also plotted.

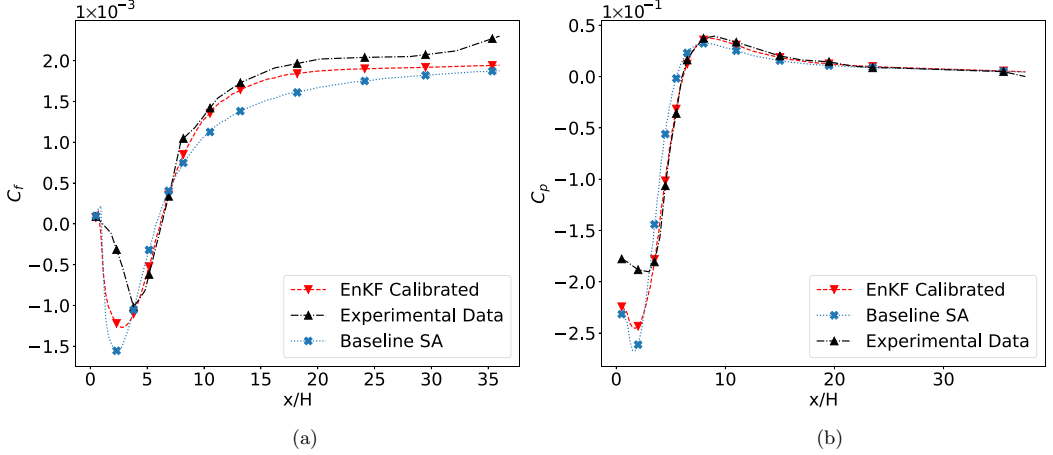


FIG. 5. BFS: (a) C_f , (b) C_p vs x/H . The calibrated SA shows improvement in both the recovery zone and the separation bubble as compared to the baseline model. The improvement in this case is defined as proximity to the experimental results.

The mean of the members of the posterior X^P is obtained as follows: $b = 1.39$, $\sigma = 0.97$, $C_{w2} = 0.78$, $C_{w3} = 0.67$, and $C_{v1} = 8.24$. The plots of C_{b1} and f_w using the calibrated coefficients are given in Figs. 4(a) and 4(b). In Fig. 4(b), the mapping (NN) of f_w from the study of Bin *et al.* [36] is also compared to the current mapping. From here it can be concluded that the f_w in Eq. (3) provides enough flexibility to learn new mappings by changing C_{w2} and C_{w3} . In terms of computational costs, each of the 30 iterations utilized five different sets of SA coefficients, resulting in 150 CFD runs on a mesh with approximately 13 000 cells for the BFS. The calibration was parallelized by assigning one core to each of the five CFD simulations. Although the parallelization used in this study is relatively straightforward, improved load-balancing methods can be employed to accelerate convergence.

IV. RESULTS

In this section, the calibrated model is tested for various flows. The tested flows are classified into three categories: separated, attached, and unbounded. The calibrated model is evaluated for improved performance on separating flows while retaining the same good performance in attached and unbounded flows.

A. Separated flows

In this section, three separated flows are analyzed, namely BFS [41], 2D-WMH [42], and BFS2 (changed step height) [36,43].

1. Flow over a BFS

In this section, the results for the flow over BFS are outlined. This flow was also used to calibrate the SA model using a relatively coarser mesh (≈ 13 000 cells). The testing was done on multiple finer meshes (Mesh 1–4), ≈ 28 000, 43 000, 47 000, and 53 000 cells. These test cases also serve as a good indicator for the soft evaluation of the calibration across different meshes. Here, mesh 1 (28 000 cells) is tested, while Appendix C covers the rest of the test cases.

Figure 5 compares the C_f and C_p plots from the calibrated SA model with that of the original SA; experimental data are also plotted for the purpose of comparison. It can be seen that the calibration significantly improves the results for the SA model, i.e., the results are closer to the experimental

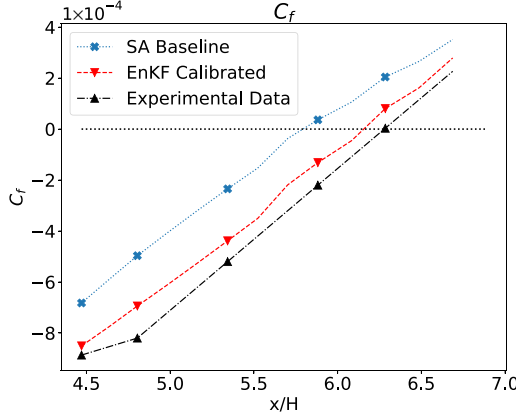


FIG. 6. BFS: C_f vs x/H showing the improved reattachment location ($C_f = 0$) for the calibrated model.

data used for calibration. Figure 5(a) shows that the C_f in the recovery zone is more accurately predicted by the calibrated model. In addition, there is a significant improvement in the magnitude of the C_f in the separation bubble. Similar improvements are also observed in C_p [Fig. 5(b)]. The reattachment length in the calibrated model is also closer to the experimental values, as shown in Fig. 6. Further analysis suggested that each coefficient of calibrated SA impacted improvement in the results in a very specific manner. Notably, C_{b1} and $f_w(C_{w2}, C_{w3})$ influenced the separation and recovery zone, respectively. The effect is more evident in C_f , hence Fig. 7 shows only the results for C_f .

As shown in Fig. 7, if the baseline value of $C_{b1} = 0.1355$ was used while using the calibrated values for the rest of the coefficients, the improvement is mainly observed in the recovery zone, while the separation zone remains similar in magnitude to the baseline SA model. On the contrary, if baseline $f_w(C_{w2}, C_{w3})$ is used in combination with the rest of the calibrated coefficients, the separation zone improves while the recovery zone remains closer to the baseline SA. However, the

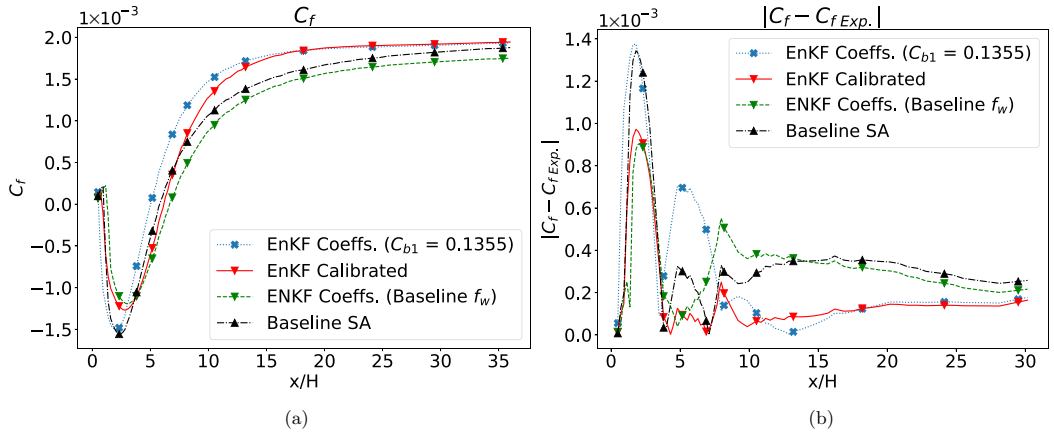


FIG. 7. BFS: (a) C_f vs x/H showing the impact of C_{b1} and f_w individually on the calibration results. If baseline C_{b1} is used along with the rest of the calibrated values (dotted blue), the results only show improvement in the recovery zone, while remaining almost similar in the separation bubble. On the other hand, if baseline $f_w(C_{w2}, C_{w3})$ is used along with the rest of the calibrated coefficients (dashed green), the improvement is mainly observed in the separation zone, while the results in the recovery zone remain close to the baseline SA. (b) Absolute error with respect to the experimental data for each configuration vs X/H .

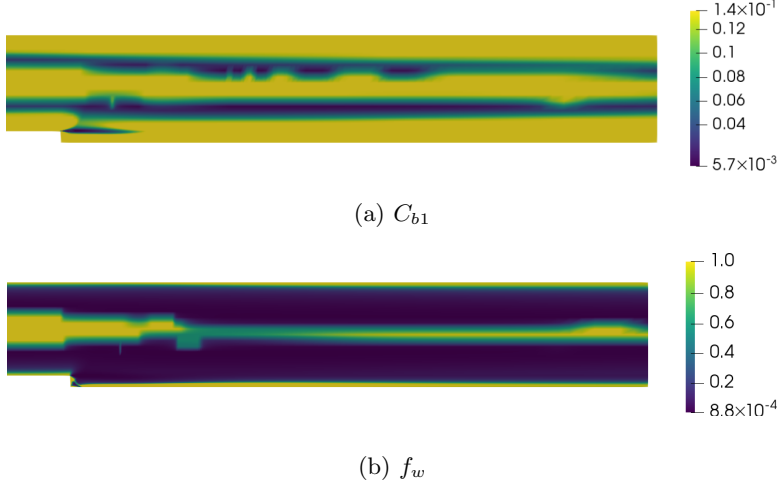


FIG. 8. BFS: Variation of C_{b1} and f_w in the domain. Note that the original C_{b1} possesses a constant value throughout the domain.

best results are obtained by using all of the calibrated coefficients. These results are consistent with the observation of Bin *et al.* [36] who used f_w as NN to calibrate the SA model while keeping the rest of the values identical. They also observed an improved recovery zone with a slight reduction of accuracy in the separation zone.

From Fig. 7, it is evident that C_{b1} and f_w have a domain-specific effect. To gain a further understanding of how these coefficients vary throughout the domain, we provide contour plots in Fig. 8. The C_{b1} takes particularly low values near the separation zone. It can also be observed that the trends of C_{b1} and f_w are almost opposite to each other throughout the domain. This opposite trend shows correlation between C_{b1} (production) and f_w (destruction). We may also gather that instead of putting the onus of balancing region-based production and destruction solely on the f_w as in the baseline model, the current formulation involves $C_{b1}(r)$ working with f_w to balance these quantities.

2. 2D-WMH

The 2D-WMH is a standard flow geometry in the NASA turbulence repository [46]. The results for the 2D-WMH are plotted in Fig. 9. The flow is attached to the bump up to $x/C = 0.655$, after which separation is observed. In Figs. 9(a) and 9(b), until separation, the SA baseline and the calibrated model are in good agreement with each other as well as with experimental data [42,46]. This agreement is encouraging as the calibration did not distort the performance of the data-enhanced model in the attached flows. Furthermore, the calibrated model shows better recovery characteristics for C_f for $x/C > 1$. Overall, in Fig. 9(b), the C_p data from the calibrated model show a good agreement with experimental data. There are some deviations observed around $0.7 < x/C < 1$. However, it can be concluded that the calibrated model C_f predictions are in better agreement with the experimental data as compared to the baseline case. On the other hand, the C_p predictions are slightly worse than the baseline model.

Similar to Fig. 7, a parametric analysis was also done for the 2D-WMH case, as shown in Fig. 10. The results show similar trends to Fig. 7, which is encouraging for consistency and generalization of the calibrated model. As observed previously, the C_{b1} affects the separation zone while f_w affects the recovery zone. In Fig. 10, choosing $C_{b1} = 0.1355$ (original value) while keeping other values from the calibration results in faster recovery of C_f , implying the effect of the calibrated coefficients (f_w) on the recovery zone. On the contrary, using a baseline f_w with other coefficients being calibrated

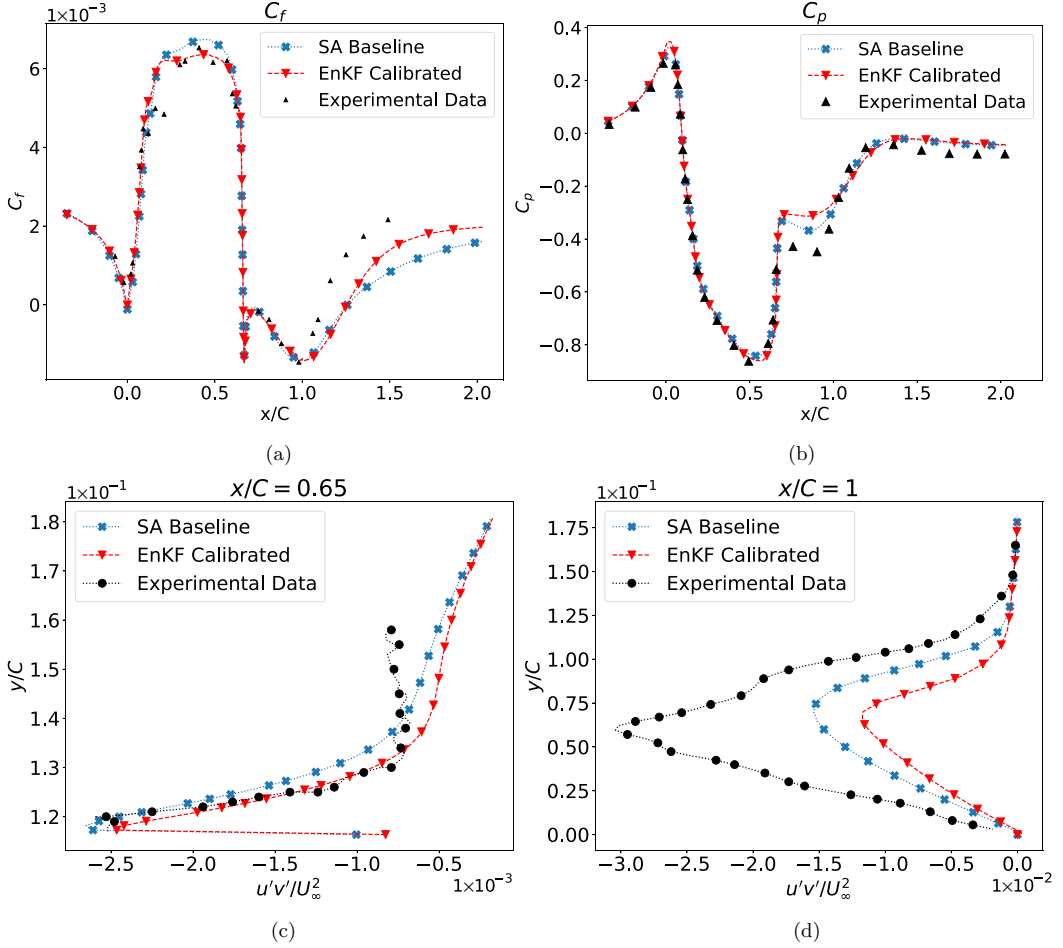


FIG. 9. 2D-WMH: (a) C_f , (b) C_p vs x/C , where C is the chord length of the bump. Parts (c) and (d) show the $u'v'/U_\infty^2$ vs y/C at location $x/C = 0.65$ and 1, respectively. The $u'v'/U_\infty^2$ for the calibrated model matches the experimental data for $x/C = 0.65$, i.e., separation. For $x/C = 1$, both models have a significant deviation from the experimental data, however the SA model is slightly better.

shows a very slow recovery. Figure 11 shows the contour plots of C_{b1} and f_w for the 2D-WMH. As with the BFS case (Fig. 8), the C_{b1} and f_w also follow an opposite trend to each other. The C_{b1} takes lower values near the separation zone and increases to 0.1355 downstream of the bump.

3. Flow over backward-facing step (changed height, BFS2)

The calibrated model was further tested on a new backward-facing step case with a changed step height and $Re \approx 5600$ [36,43]. The case is derived from the study of Bin *et al.* [36], who also used to test it for their DNS-calibrated SA model. The step height is 2 m i.e., half of the domain height and $Re \approx 5600$. Figure 12 compares the agreement of C_f from calibrated and baseline SA with that of DNS from Bin *et al.* [36]. In addition, the results of the Bin *et al.* model are also presented for comparison. The results of Fig. 12 show better agreement of C_f between our calibrated model and DNS when compared to the baseline SA model. In addition, the results show a better accuracy of the current calibrated model in the recirculating zone than the Bin *et al.* [36] calibrated model. The better results in the recirculation zone are attributed to the calibration of C_{b1} in addition to other

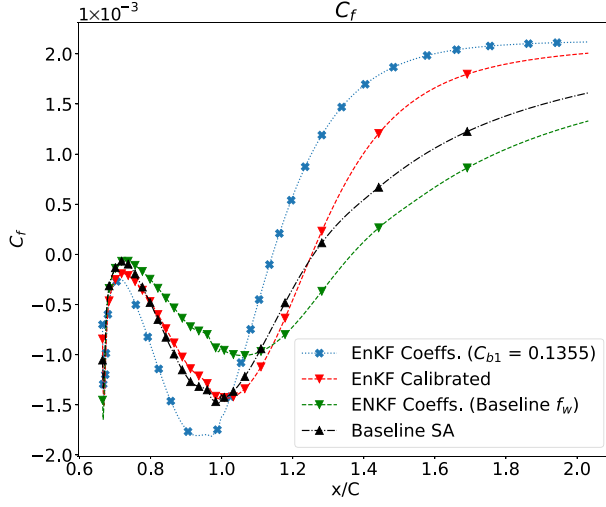


FIG. 10. 2D-WMH: C_f vs x/C , plotted after the separation point $x/C > 0.655$. Parametric analysis of calibrated coefficients by using baseline values in C_{b1} and f_w alternatively. The dotted blue line shows C_f where the calibrated coefficients are paired with C_{b1} . The dashed green line shows the calibrated coefficients paired with baseline f_w . The red and black lines show the results from calibrated and baseline models, respectively.

coefficients, whereas Bin *et al.* [36] only calibrate f_w in their study. For further establishing the role of C_{b1} and f_w on C_f , a similar analysis to Figs. 7 and 10 is performed in Fig. 13. The results are consistent with the previous results, i.e., C_{b1} affects the accuracy in the recirculating zone, whereas the f_w effect is predominant in the recovery zone.

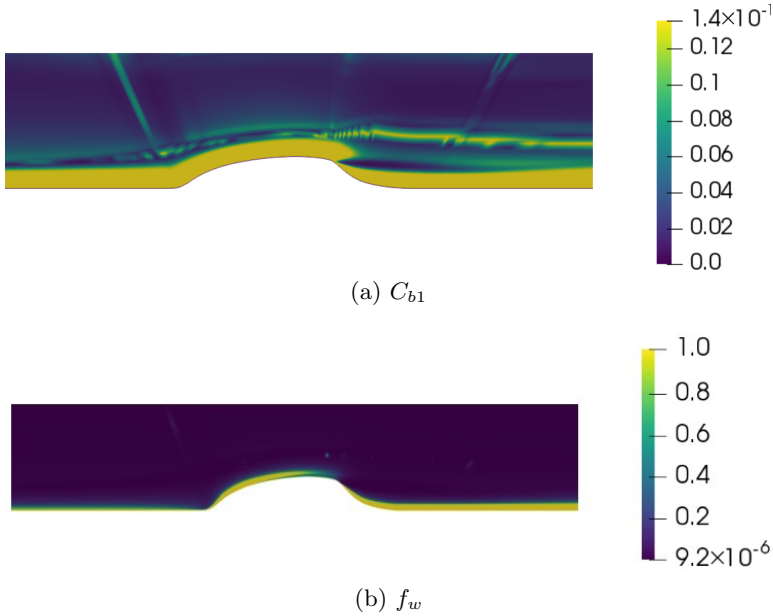


FIG. 11. 2D-WMH: Variation of C_{b1} and f_w in the domain.

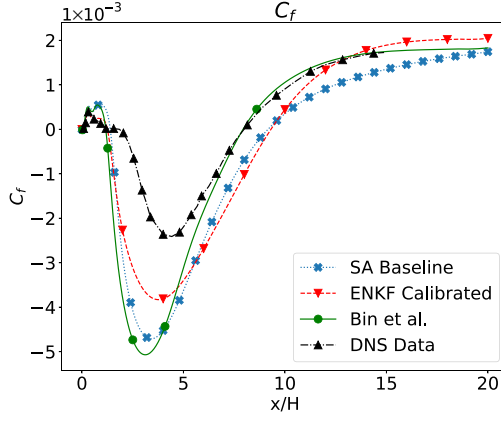


FIG. 12. BFS2: C_f vs x/H along the bottom wall obtained from the calibrated coefficients is compared with DNS [36] and baseline SA. Additionally, the data from the calibrated SA model of Bin *et al.* [36] are also given.

B. Unbounded or attached flow

We have established that the EnKF-based calibration improves the SA model's performance in separated flows. However, the change in model parameters may distort the good performance of the model in unbounded or attached flows. In this section, the calibrated model is compared with the original SA model to measure any deviation.

1. NACA0012

The model is first tested for an unbounded flow over an NACA0012 airfoil at the angles of attack 0° and 10° in Figs. 14 and 15, respectively [47,48]. The calibrated model shows a good agreement with the original SA model with minimal distortions, and we conclude that the performance of the

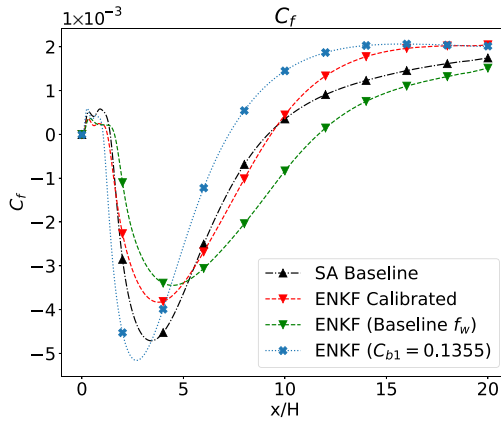


FIG. 13. BFS2: Parametric analysis plotting C_f vs x/H along the bottom wall post step. The dashed green line displays the baseline f_w combined with the rest of the EnKF calibrated coefficients, maintaining the initially observed improvement (Fig. 12) within the recirculation zone but with a reduction in the recovery zone. Conversely, the dotted blue line depicts the baseline ($C_{b1} = 0.1355$) along with the rest of the calibrated coefficients, sustaining the improvement in the recovery zone but a decrease in the recirculation zone.

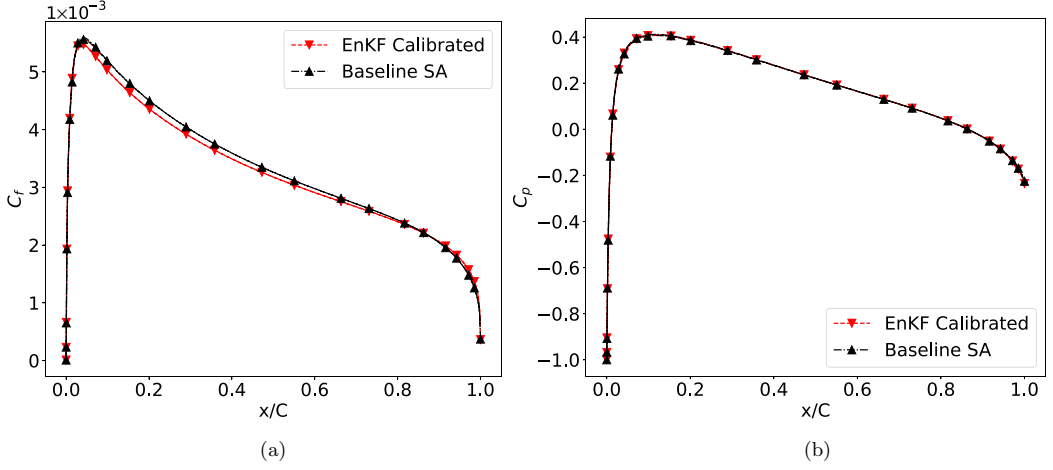


FIG. 14. NACA0012 airfoil at an angle of attack 0°: (a) C_f , (b) C_p vs x/C . The calibrated model shows good agreement with the original model. Hence, no distortion in good behavior of the SA model is observed for unbounded flows over an airfoil.

original model is preserved in the calibrated variant. Furthermore, a comparison of the lift (C_l) and drag (C_d) coefficients was also made. For 10°, the C_l was ≈ 1 , and C_d was ≈ 0.013 for both models. For 0°, the C_d was ≈ 0.008 , and C_l was ≈ 0.001 for both models. This demonstrated a minimal deviation from the base SA performance for the NACA0012 case.

2. Flat plate boundary layer

The improved model was further tested on a zero pressure gradient flat plate boundary layer flow to determine any distortion from the standard SA model in attached flows. Figures 16(a) and 16(b) show the C_f and C_p versus Re_x plots for the calibrated and baseline model. It can be seen that the results for baseline and the calibrated model are in good agreement, while having slight distortions. Figures 16(c) and 16(d) show the difference between baseline and the calibrated model for C_f and C_p . Additionally, Fig. 17 shows U^+ versus y^+ plotted at $Re_\theta \approx 8000$ for both models. It can be seen

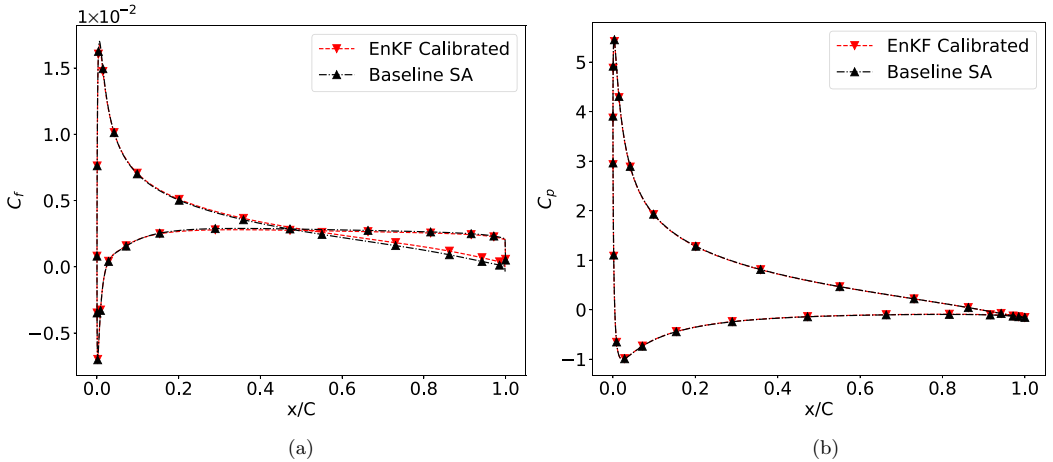


FIG. 15. NACA0012 airfoil at an angle of attack 10°: (a) C_f , (b) C_p vs x/C .

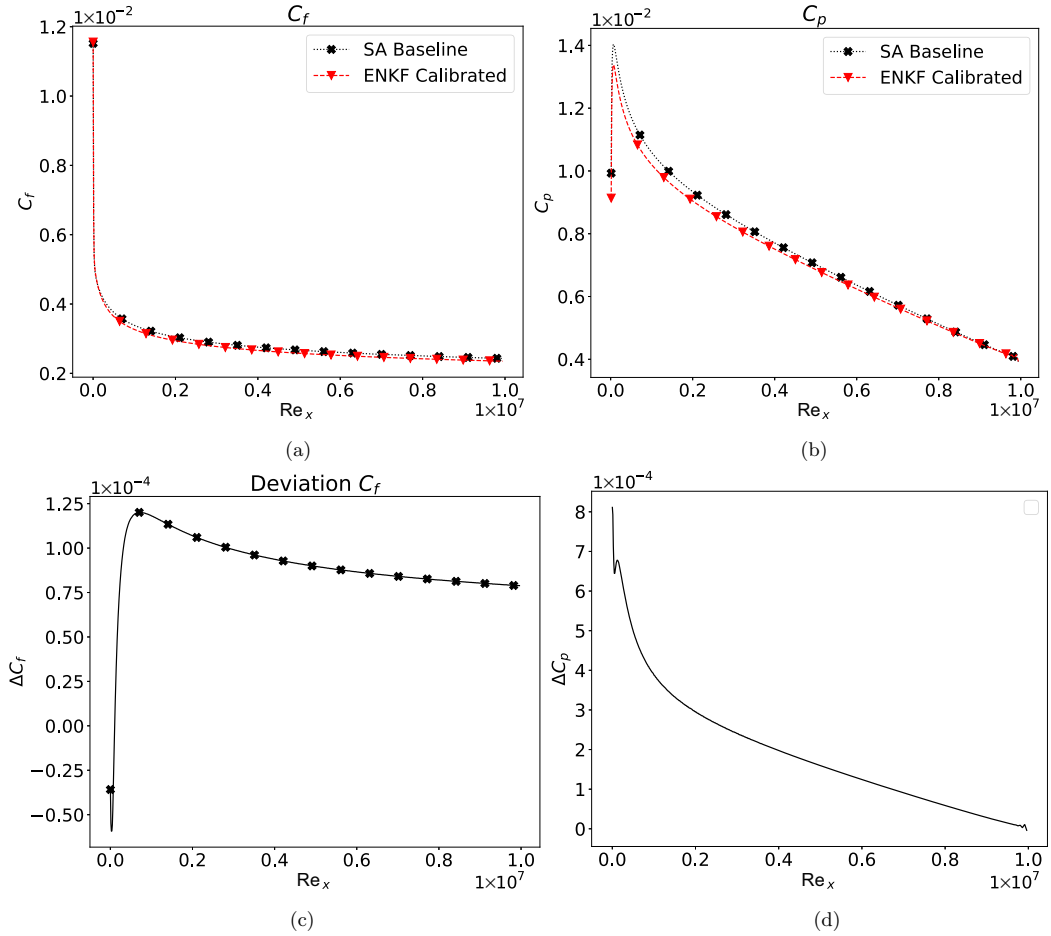


FIG. 16. Zero pressure gradient boundary layer: (a) C_f , (b) C_p vs Re_x for flow over a flat plate showing agreement in the behavior of the calibrated model for attached flows. Parts (c) and (d), respectively, show a deviation between the two models for C_f and C_p .

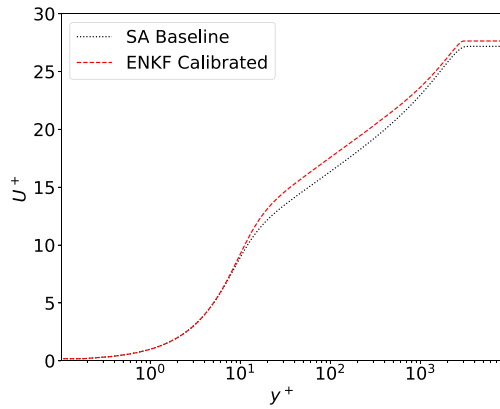


FIG. 17. Zero pressure gradient boundary layer: U^+ vs y^+ for both models.

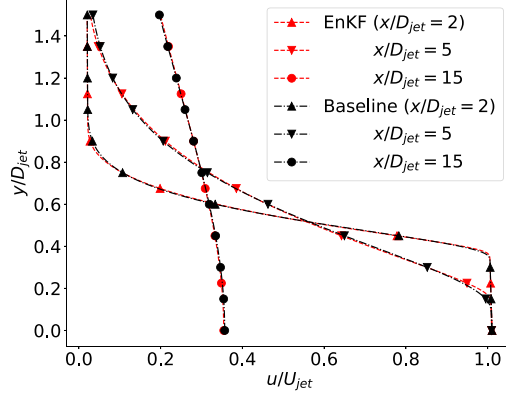


FIG. 18. ASJ: u/U_{jet} vs y/D_{jet} along $x/D_{\text{jet}} = 2, 5$, and 15 , obtained from the calibrated coefficients, is compared with baseline SA. Here, $D_{\text{jet}} = 50.8$ mm is the diameter of the jet, and U_{jet} is the velocity at the center of the jet exit.

that both models agree well. From here, it can be inferred that the calibrated SA model does not significantly distort the behavior of the baseline model in attached or unbounded flows.

3. Axisymmetric jet

The calibrated model is further tested on the free shear flow, i.e., an axisymmetric jet (ASJ) [49,50]. This test will further provide insights into the calibrated model's behavior for (r) close to zero. The primary objective of the ASJ test is to assess whether the calibrated model can accurately capture the behavior of the original SA model for ASJ conditions. In Fig. 18, the velocity profile (u/U_{jet}) is plotted against radial distance (y/D_{jet}) for various axial positions ($x/D_{\text{jet}} = 2, 5$, and 15). The results from the EnKF model closely align with those from the original SA (baseline) model.

4. Mixing layer (MIXL)

For further validation, the calibrated model was also tested on a classical mixing layer test case. Figure 19 shows the results of the velocity profile at two x locations. Here, U is the velocity, U_1 is the lower inlet velocity, and ΔU is the difference between the velocity of the upper and lower

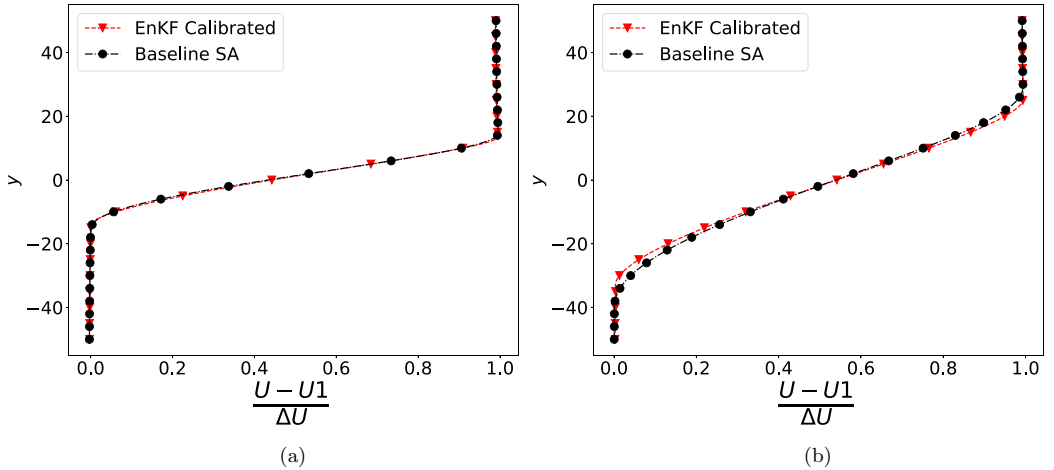


FIG. 19. MIXL: U vs Y for the mixing layer showing good agreement between calibrated and baseline SA.

inlets. It can be seen that the results are in good agreement, with some minor distortion towards the extremes. This further illustrates that the calibrated model recovers SA performance on classical test cases.

V. CONCLUSIONS

An EnKF-based calibration methodology has been introduced for improving RANS closure models with limited and noisy experimental data. This study's focus was on the calibration of SA model for cases where sparse, quantity-of-interest experimental data may be available. The SA coefficients were effectively adjusted using a simple parametrization, potentially minimizing the need for black-box ML models like NNs, which may fail to generalize. The calibrated SA model exhibited improved accuracy in predicting important flow quantities, specifically C_p and C_f , in scenarios involving separated flows. Notably, this improvement was achieved without compromising the SA model's accuracy in predicting behavior in attached and unbounded flows, aligning well with the progressive nature of SA enhancements.

The findings further corroborate the hypothesis put forth in Ref. [9], demonstrating that a substantial portion of closure model errors can be rectified by coefficient adjustments. The calibration process utilized only one geometry, namely BFS, at a single Re . Due to the generalization provided by the SA model, this approach successfully extended the calibrated model's applicability to extrapolated cases and scenarios beyond its training range. In contrast, such stringent training criteria could lead to overfitting and extrapolation in the context of deep neural network applications. The adaptability of the original f_w function Eq. (3) was also evident in this study, as the calibrated C_{w2} and C_{w3} coefficients displayed trends similar to those captured by a trained NN [as seen in Fig. 4(b)]. Another notable advancement involved the treatment of C_{b1} as a function of r instead of a fixed scalar value found in the baseline SA model. This increased flexibility in representing C_{b1} notably enhanced the calibrated model's predictive capabilities within recirculation zones. The interplay between C_{b1} and f_w was also evident, where the former significantly impacted recirculation zone predictions while the latter influenced recovery zone predictions.

The stochastic nature of the EnKF necessitated a thoughtful selection of coefficient sampling ranges, a process guided by a parametric analysis (Appendix A). This range determination was intricately hinged on an understanding of the relationships between production, destruction, and diffusion terms. Nonetheless, the possibility of relaxing this selection criterion through calibrations with multiple flow conditions remains a viable avenue for future exploration within the study's scope.

ACKNOWLEDGMENTS

We gratefully acknowledge the insights provided about the Spalart-Allmaras turbulence model by Dimitrios Fytanidis at Argonne National Laboratory. This material is based upon work supported by the U.S. Department of Energy (DOE), Office of Science, Office of Advanced Scientific Computing Research, under Contract No. DE-AC02-06CH11357. This research was funded in part and used resources from the Argonne Leadership Computing Facility, which is a DOE Office of Science User Facility supported under Contract No. DE-AC02-06CH11357. R.M. acknowledges support from DOE-ASCR-2493—"Data-intensive scientific machine learning."

APPENDIX A: PARAMETRIC ANALYSIS FOR THE SA MODEL

In this Appendix, a parametric analysis by varying the SA coefficients is performed. The underlying objective is to enhance our comprehension of how alterations in coefficient values influence the QOIs, such as C_f and C_p , in the context of separation phenomena. This analysis contributes significantly to the selection of coefficients, along with their respective bounding values,

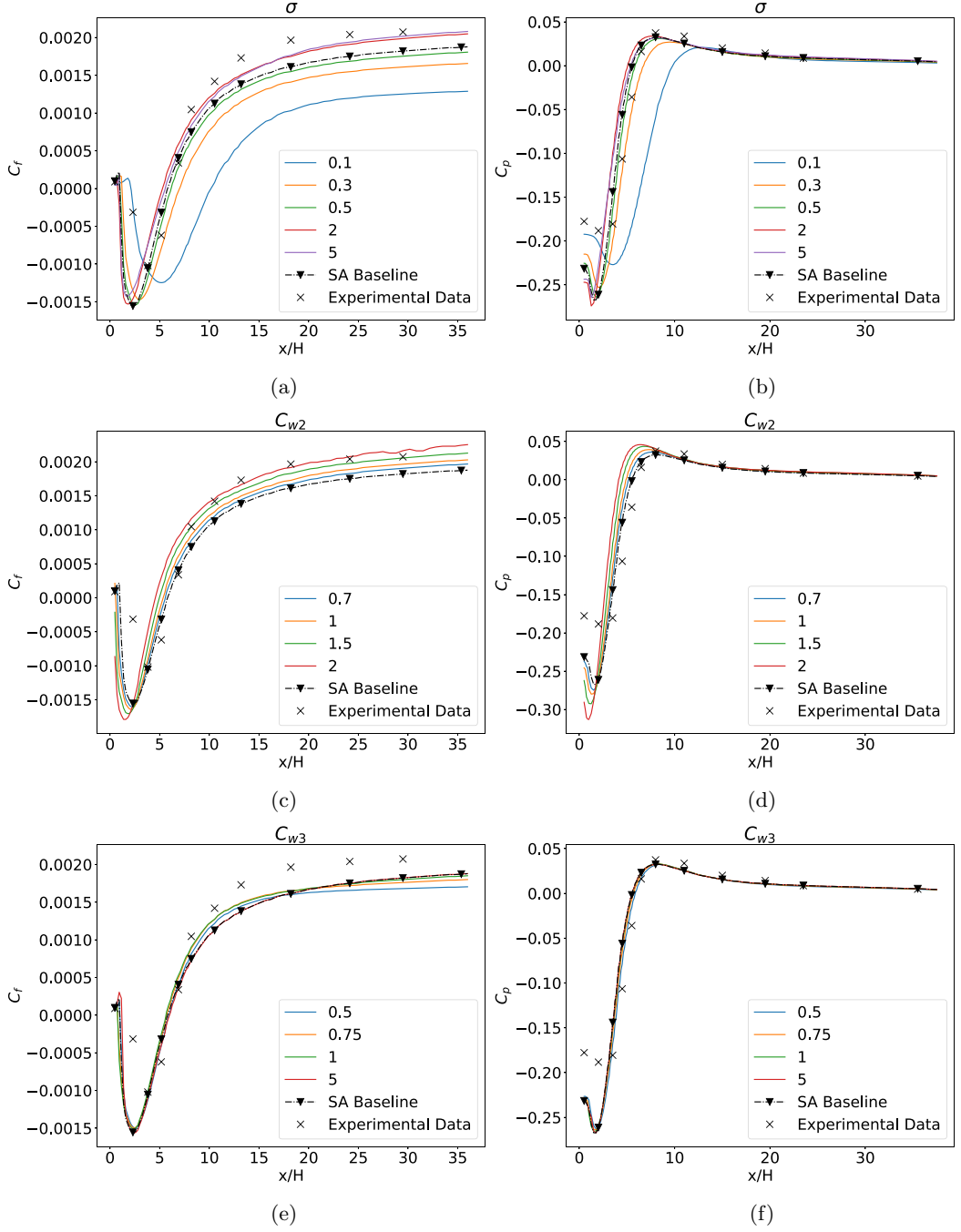


FIG. 20. Parametric analysis for C_f and C_p along the bottom wall of the BFS by varying σ (a), (b), C_{w2} (c), (d), and C_{w3} (e), (f). For reference, the solutions with the original SA coefficients along with experimental data [45] are also given. The title of each subplot is the SA coefficient that was varied for analysis.

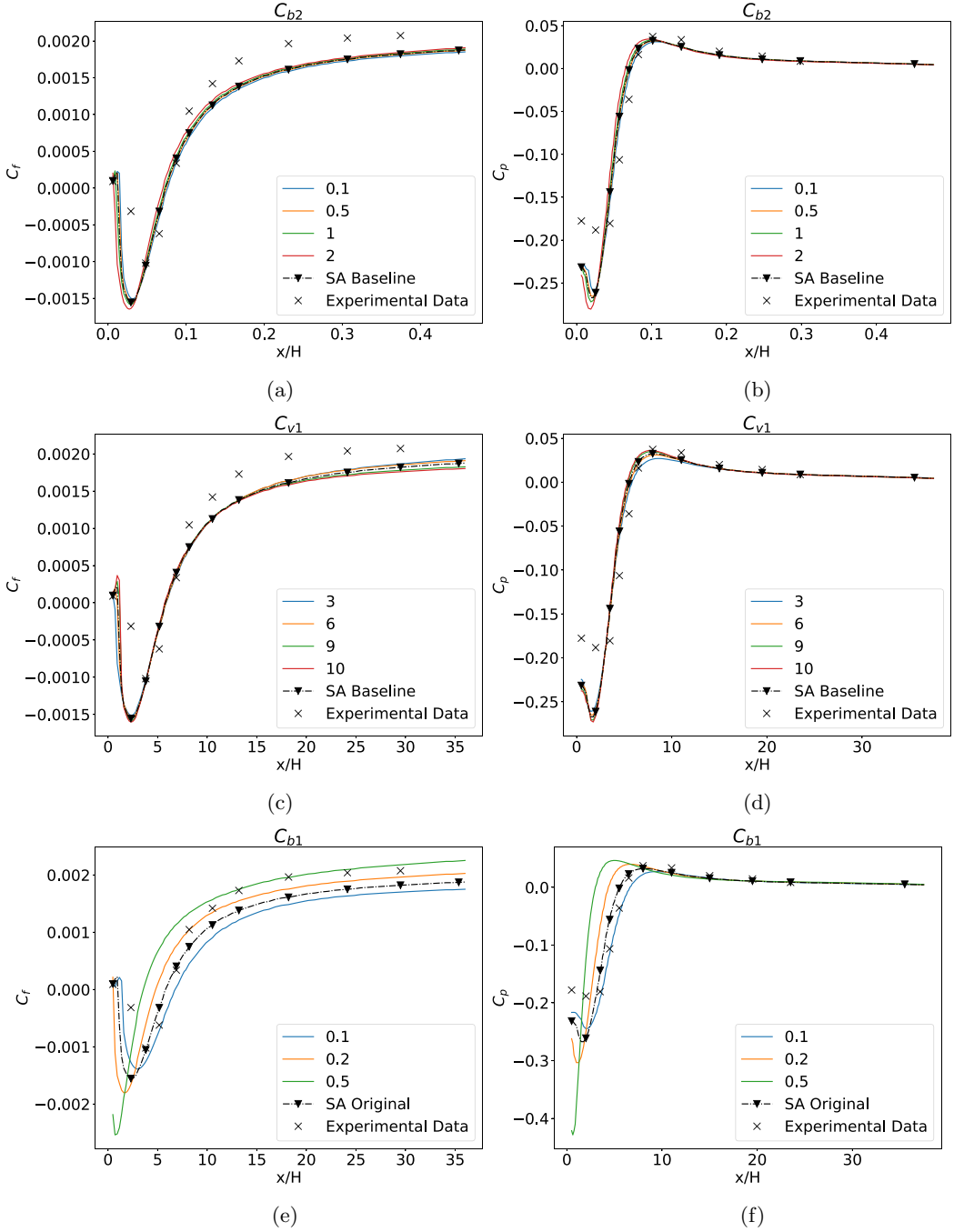


FIG. 21. Parametric analysis by varying C_{b2} (a), (b), C_{v1} (c), (d), and C_{b1} (e), (f). For reference, the solutions with the original SA coefficients along with experimental data [45] are also given.

that collectively constitute the formulation of the matrix X . Figures 20 and 21 outline the results of the analysis.

Figures 20(a) and 20(b) present the variations in C_f and C_p with different σ values. The parameter σ influences the diffusivity within the SA equation. Notably, observable changes in both C_f and C_p

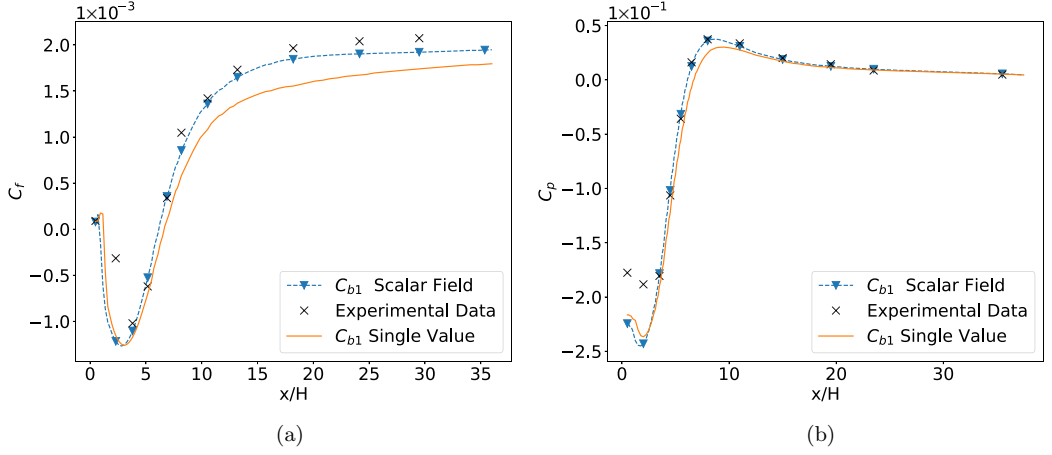


FIG. 22. Comparison of EnKF calibration using C_{b1} as a function of r with C_{b1} as constant scalar within the BFS domain. (a) C_f and (b) C_p along the bottom wall for both calibrations.

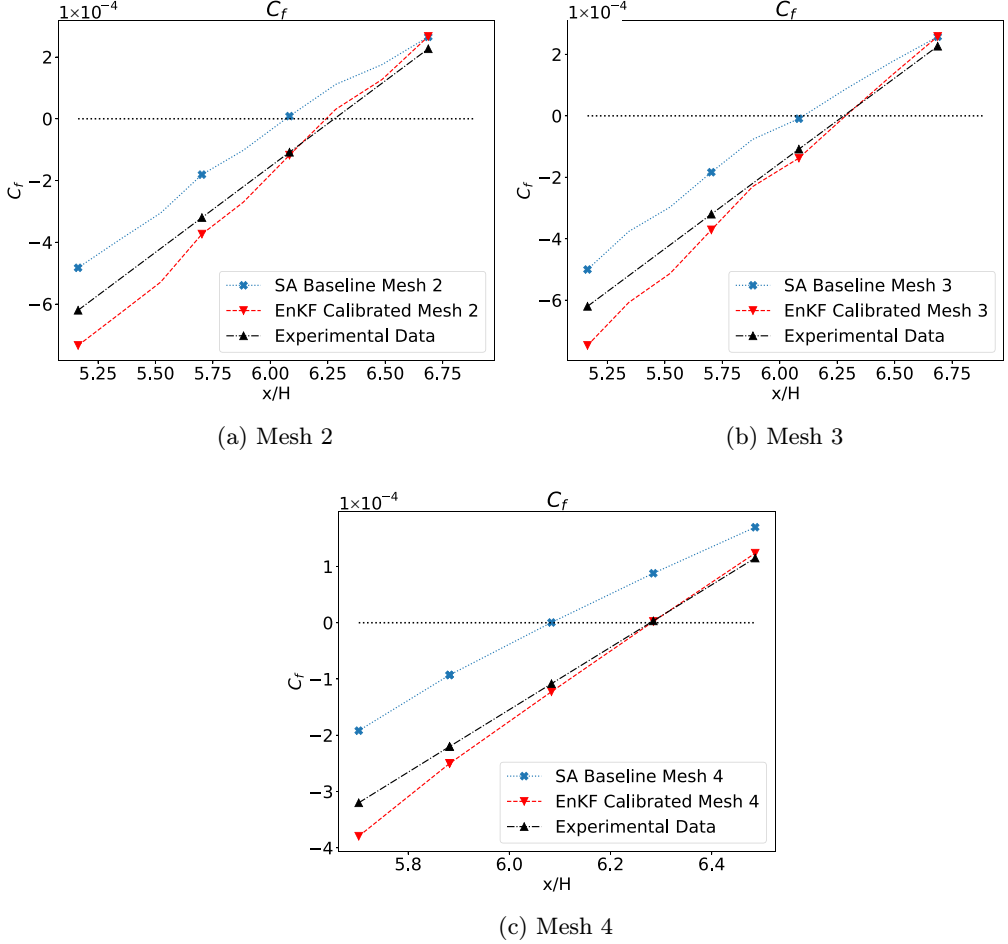
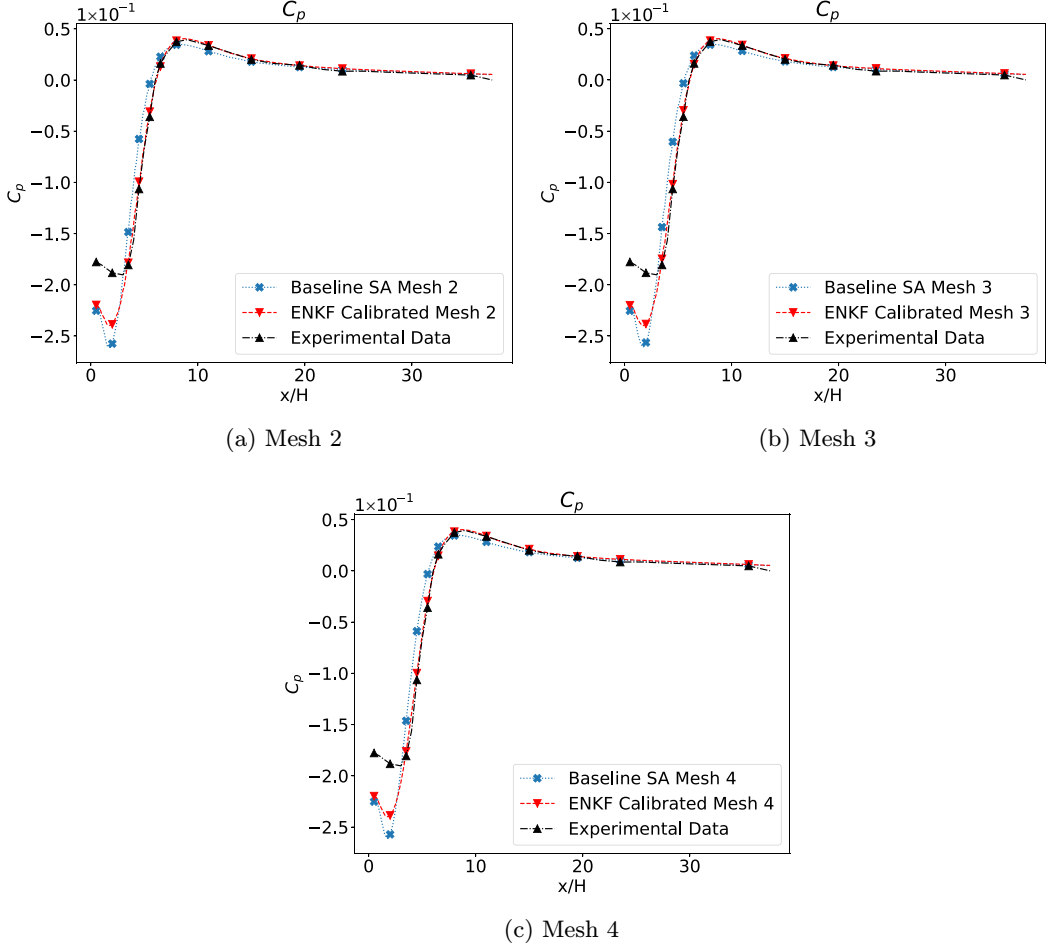


FIG. 23. C_f vs x/H showing the improved reattachment location ($C_f = 0$) for the calibrated model across meshes 2-4.


 FIG. 24. C_p vs x/H across meshes 2–4.

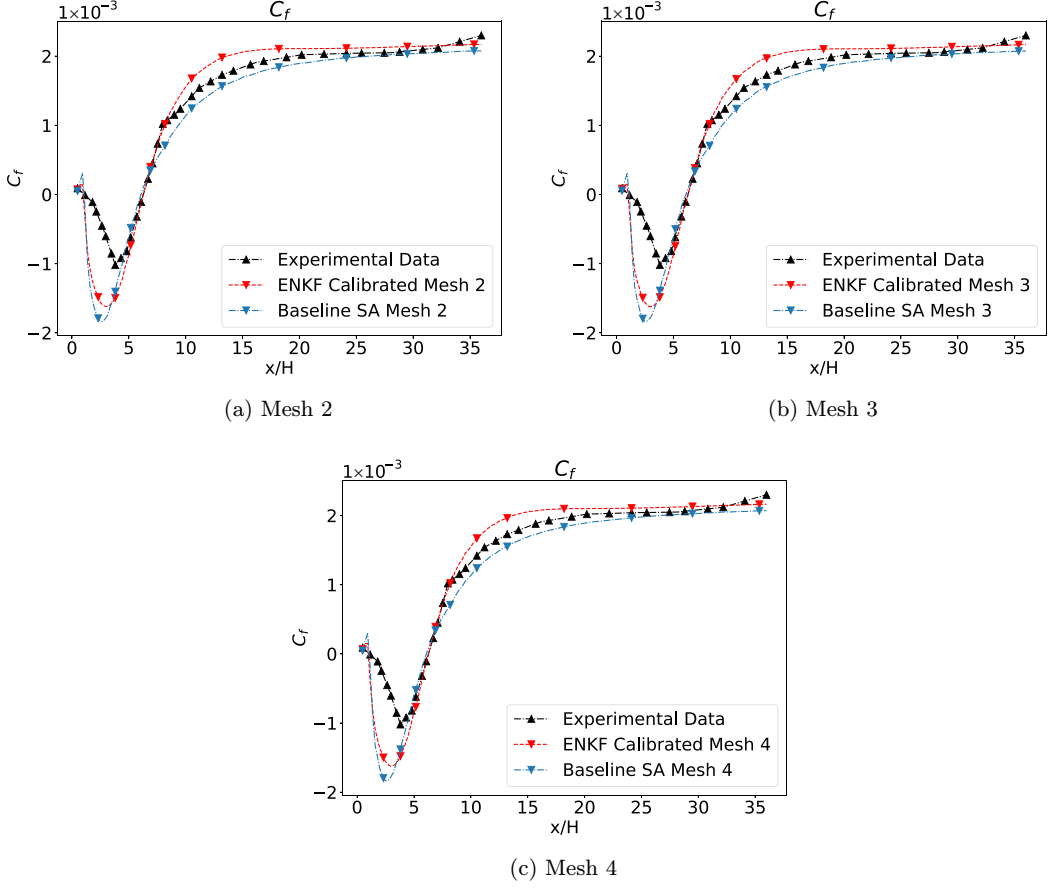
occur in response to alterations in σ values. Consequently, the choice of σ assumes importance as a target for optimization in EnKF.

The range $\sigma \in [0.3, 2]$ yields results in the vicinity of experimental data. Values below 0.3, such as $\sigma = 0.1$, deviate substantially from the experimental data, while $\sigma = 5$ displays minimal variance compared to the results at 2. This lack of variation at $\sigma > 2$ does not incentivize an expansion of the sample space. Hence, the interval $[0.3, 2]$ emerges as the preferred range for σ sampling in the X matrix.

Figures 20(c)–20(f) show the variation of C_f and C_p with respect to C_{w2} and C_{w3} . These two coefficients collectively contribute to the parameter f_w as depicted in Eq. (3). This parameter plays a pivotal role in governing the destruction of eddy viscosity.

The selection of C_{w2} and C_{w3} for the X matrix stems from their direct influence on f_w . Notably, f_w affects the SA's predictions for wall-bounded nonequilibrium flows [1,19,36]. Particularly, Bin *et al.* [36] outline the impact of f_w on the behavior of skin friction coefficient (C_f) in the recovery zone.

The interval $[0.75, 1.75]$ is chosen for sampling C_{w2} . This range is chosen because for different regions, the values of C_f and C_p improve based on the values C_{w2} . In addition, C_p and C_f follow mutually opposite trends for the increase or decrease of the C_{w2} . It was observed that for the values


FIG. 25. C_f vs x/H across meshes 2–4.

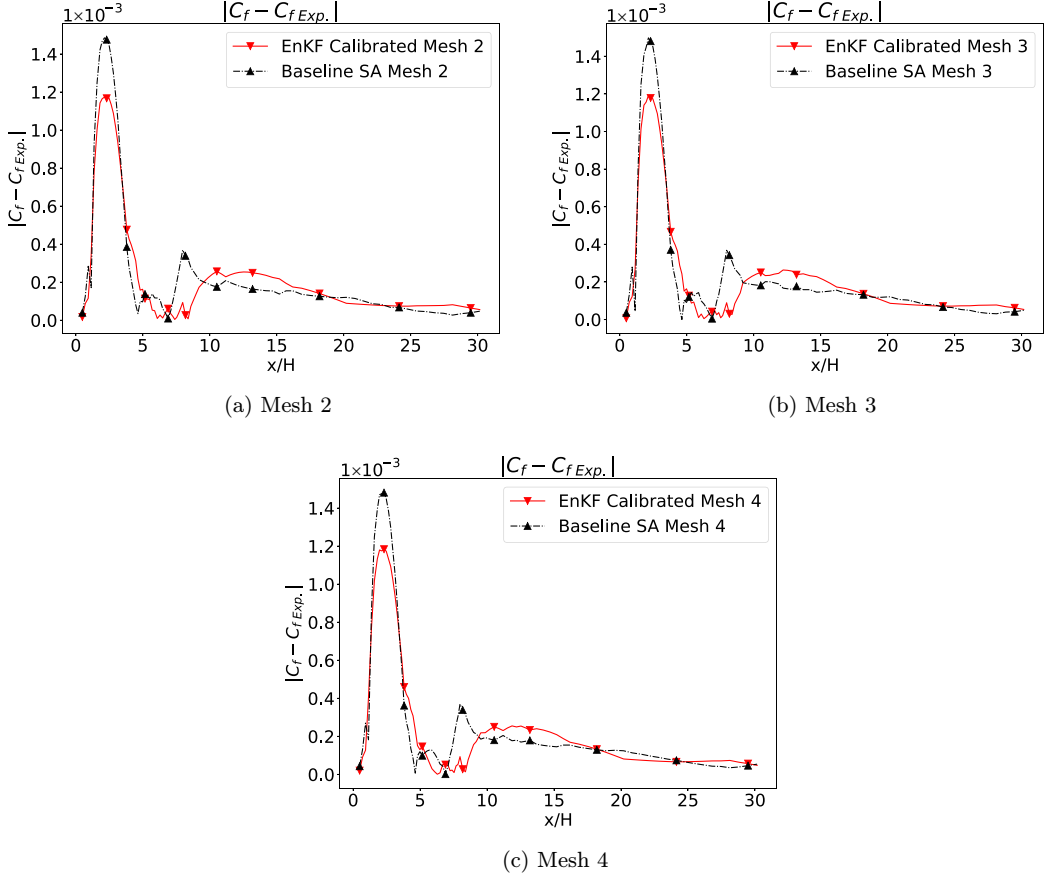
in the range $[0.75, 1.75]$, the QOI takes the values that are closer to the experimental data for the entire region.

Similarly, the interval $[1, 2]$ is decided for the C_{w3} . A slight improvement in the recovery zone for C_f is observed at $C_{w3} = 1$, which is also selected as the lower bound of the sample space due to deteriorated accuracy at $C_{w3} < 1$ at $x/H > 25$, i.e., 0.75 and 0.5. For the upper limit, the value of 2 (SA baseline) is selected due to the nonobservable difference between the results at the values of 2 and 5. Additionally, the upper bound is motivated by the original value of $C_{w3} = 2$ in the SA model.

Figures 21(a) and 21(b) depict the results of a parametric analysis involving the variation of C_{b2} . The observed variations in both C_f and C_p due to changes in C_{b2} are not substantial. Consequently, C_{b2} is not deemed influential enough to warrant selection for the optimization process.

Similarly, Figs. 21(c) and 21(d) illustrate the impact of variations in C_{v1} on C_f and C_p . Although alterations in C_{v1} have a limited effect on both coefficients, discernible variations emerge in the far downstream region for C_f and the recovery region for C_p . As a result of these observations, C_{v1} is chosen for the optimization process. For the optimization of C_{v1} , the selected range of variation is $[6, 9]$. This range is informed by the improved performance of C_f at higher values of C_{v1} . Hence, the sample space is slightly biased towards values higher than baseline $C_{v1} = 7.1$.

Figures 21(e) and 21(f) show the significant influence of varying C_{b1} on C_f and C_p . Therefore, C_{b1} is also selected for the optimization. However, for the purpose of this study, the C_{b1} is further parametrized as a function of r , where $r \equiv \nu_t / Sk^2 d^2$.


 FIG. 26. $C_f - C_{f,Exp.}$ vs x/H across meshes 2–4.

APPENDIX B: PARAMETRIZATION OF C_{b1}

From Fig. 21(e), it becomes evident that when $C_{b1} = 0.1$, the behavior of skin friction coefficient (C_f) in the re-circulation region aligns more closely with the experimental data. Conversely, with $C_{b1} = 0.2$, better performance is observed in the recovery zone. While this region-specific impact is observable for other coefficients as well, it is particularly pronounced in the case of C_{b1} . Hence, C_{b1} is parametrized further. This extension allows C_{b1} to adopt different values contingent on the flow and domain characteristics. Drawing inspiration from Eq. (3), which parametrizes f_w in terms of r , it was deemed appropriate to express C_{b1} as a function of r as well. Though the rest of the coefficients can also be parametrized further, for our study only C_{b1} is parametrized.

For the sake of simplicity, our study parametrized C_{b1} as a linear function of r , as shown in Eq. (B1). The upper bound C_{b1} is limited to its default value of 0.1355 using a min function. This upper bound has the effect of plateauing on the C_{b1} function, which is similar to the f_w . This will help to ensure the consistency between the production and destruction term of the SA model, along with preserving the behavior of the model in equilibrium flows. As in Sec. IIID, the $\max(c * r + d)$ term spikes the value for C_{b1} as r approaches zero; this is important for maintaining the behavior of the model in free shear flows. The simplistic nature of Eq. (B1) and the improvements due to it are encouraging. However, the equation used here is not claimed to be optimum for the parametrization, and it mildly violates the soft constraint proposed by Spalart *et al.* [19] for the data-driven studies, i.e., not using min or max functions. Hence, a more focused study can be conducted

to explore equations that are more consistent with the SA model. Another approach could be to replace Eq. (B1) by a NN,

$$C_{b1} = \min(\max(r * b, c * r + d), 0.1355). \quad (\text{B1})$$

Figure 22 compares the EnKF calibration for both scenarios, i.e., where the C_{b1} is (i) a scalar field varying with respect to r , and (ii) a acalar field with a constant value throughout the domain. Notably, the rest of the coefficients in the ensemble are the same. Using C_{b1} as a function of r yields results closer to the experimental values and hence was the preferred approach for the current study.

APPENDIX C: BACKWARD-FACING STEP (BFS): MESH 2-4

In this Appendix, the previously calibrated coefficients tested for meshes 2–4 (Sec. IV A 1), approximately 43 000, 47 000, and 53 000 cells, respectively, are outlined for the BFS. Figure 23 shows the reattachment location of the calibrated model compared to the baseline for each mesh, along with the experimental data. It is evident that the reattachment location is significantly improved for each mesh compared to the baseline SA model.

Figure 24 presents the C_p curves for each mesh. The calibrated model demonstrates better agreement with the experimental data across all meshes.

For C_f , Figs. 25 and 26, the calibrated model shows agreement with the experimental data in the separation bubble and reattachment zone.

For each mesh, Fig. 26 shows a deviation of C_f from experimental data. It can be seen that the calibrated model has better agreement with the experimental data in the separation bubble and the reattachment zone.

-
- [1] P. Spalart and S. Allmaras, A one-equation turbulence model for aerodynamic flows, in *30th Aerospace Sciences Meeting and Exhibit, Reno, NV, USA* (AIAA, Reston, VA, 1992), p. 439.
 - [2] X. I. A. Yang and K. Griffin, Grid-point and time-step requirements for direct numerical simulation and large-eddy simulation, *Phys. Fluids* **33**, 015108 (2021).
 - [3] J.-Q. J. L. Li, X. I. A. Yang, and R. Kunz, Grid-point and time-step requirements for large-eddy simulation and Reynolds-averaged Navier–Stokes of stratified wakes, *Phys. Fluids* **34**, 115125 (2022).
 - [4] P. Durbin, Some recent developments in turbulence closure modeling, *Annu. Rev. Fluid Mech.* **50**, 77 (2018).
 - [5] R. Bush, T. Chyczewski, K. Duraisamy, B. Eisfeld, C. Rumsey, and B. Smith, Recommendations for future efforts in RANS modeling and simulation, in *Proceedings of the AIAA Scitech 2019 Forum, San Diego, CA, USA* (AIAA, Reston, VA, 2019), p. 0317.
 - [6] K. Duraisamy, G. Iaccarino, and H. Xiao, Turbulence modeling in the age of data, *Annu. Rev. Fluid Mech.* **51**, 357 (2019).
 - [7] B. Tracey, K. Duraisamy, and J. Alonso, A machine learning strategy to assist turbulence model development, in *53rd AIAA Aerospace Sciences Meeting* (AIAA, Kissimmee, Florida, 2015), p. 1287.
 - [8] Y. Yin, Z. Shen, Y. Zhang, H. Chen, and S. Fu, An iterative data-driven turbulence modeling framework based on Reynolds stress representation, *Theor. Appl. Mech. Lett.* **12**, 100381 (2022).
 - [9] J. Ray, L. Dechant, S. Lefantzi, J. Ling, and S. Arunajatesan, Robust Bayesian calibration of a k- ϵ model for compressible jet-in-crossflow simulations, *AIAA J.* **56**, 4893 (2018).
 - [10] J. Li, Y. Bin, G. Huang, and X. Yang, Enhancing generalizability of machine-learning turbulence models, in *AIAA SCITECH 2024 Forum, Orlando, FL* (AIAA, Reston, VA, 2024), p. 1574.
 - [11] A. Vadrot, X. I. A. Yang, and M. Abkar, Survey of machine-learning wall models for large-eddy simulation, *Phys. Rev. Fluids* **8**, 064603 (2023).
 - [12] L. Zhu, W. Zhang, J. Kou, and Y. Liu, Machine learning methods for turbulence modeling in subsonic flows around airfoils, *Phys. Fluids* **31**, 015105 (2019).

- [13] L. Zhu, W. Zhang, X. Sun, Y. Liu, and X. Yuan, Turbulence closure for high Reynolds number airfoil flows by deep neural networks, *Aerosp. Sci. Technol.* **110**, 106452 (2021).
- [14] X. Sun, W. Cao, Y. Liu, L. Zhu, and W. Zhang, High Reynolds number airfoil turbulence modeling method based on machine learning technique, *Comput. Fluids* **236**, 105298 (2022).
- [15] R. Maulik, H. Sharma, S. Patel, B. Lusch, and E. Jennings, A turbulent eddy-viscosity surrogate modeling framework for Reynolds-averaged Navier-Stokes simulations, *Comput. Fluids* **227**, 104777 (2021).
- [16] Y. Liu, W. Cao, W. Zhang, and Z. Xia, Analysis on numerical stability and convergence of Reynolds averaged Navier–Stokes simulations from the perspective of coupling modes, *Phys. Fluids* **34**, 015120 (2022).
- [17] J. Ling, A. Kurzawski, and J. Templeton, Reynolds averaged turbulence modelling using deep neural networks with embedded invariance, *J. Fluid Mech.* **807**, 155 (2016).
- [18] S. Pope, A more general effective-viscosity hypothesis, *J. Fluid Mech.* **72**, 331 (1975).
- [19] P. Spalart, An old-fashioned framework for machine learning in turbulence modeling, [arXiv:2308.00837](https://arxiv.org/abs/2308.00837).
- [20] J.-X. Wang, J.-L. Wu, and H. Xiao, Physics-informed machine learning approach for reconstructing Reynolds stress modeling discrepancies based on DNS data, *Phys. Rev. Fluids* **2**, 034603 (2017).
- [21] J.-L. Wu, H. Xiao, and E. Paterson, Physics-informed machine learning approach for augmenting turbulence models: A comprehensive framework, *Phys. Rev. Fluids* **3**, 074602 (2018).
- [22] J. Wu, H. Xiao, R. Sun, and Q. Wang, Reynolds-averaged Navier–Stokes equations with explicit data-driven Reynolds stress closure can be ill-conditioned, *J. Fluid Mech.* **869**, 553 (2019).
- [23] R. McConkey, E. Yee, and F.-S. Lien, Deep structured neural networks for turbulence closure modeling, *Phys. Fluids* **34**, 035110 (2022).
- [24] M. Shirzadi, P. Mirzaei, and Y. Tominaga, RANS model calibration using stochastic optimization for accuracy improvement of urban airflow CFD modeling, *J. Build. Eng.* **32**, 101756 (2020).
- [25] C. Grabe, F. Jäckel, P. Khurana, and R. Dwight, Data-driven augmentation of a RANS turbulence model for transonic flow prediction, *Int. J. Numer. Methods Heat Fluid Flow* **33**, 1544 (2023).
- [26] H. Kato, K. Ishiko, and A. Yoshizawa, Optimization of parameter values in the turbulence model aided by data assimilation, *AIAA J.* **54**, 1512 (2016).
- [27] H. Kato and S. Obayashi, Approach for uncertainty of turbulence modeling based on data assimilation technique, *Comput. Fluids* **85**, 2 (2013).
- [28] J. Ray, S. Lefantzi, S. Arunajatesan, and L. Dechant, Bayesian parameter estimation of a k- ϵ model for accurate jet-in-crossflow simulations, *AIAA J.* **54**, 2432 (2016).
- [29] K. Duraisamy, Z. Zhang, and A. P. Singh, New approaches in turbulence and transition modeling using data-driven techniques, in *53rd AIAA Aerospace Sciences Meeting, Kissimmee, Florida* (AIAA, Reston, VA, 2015), p. 1284.
- [30] A. P. Singh, K. Duraisamy, and Z. J. Zhang, Augmentation of turbulence models using field inversion and machine learning, in *55th AIAA Aerospace Sciences Meeting, Grapevine, Texas* (AIAA, Reston, VA, 2017), p. 0993.
- [31] A. P. Singh and K. Duraisamy, Using field inversion to quantify functional errors in turbulence closures, *Phys. Fluids* **28**, 045110 (2016).
- [32] M. Yang and Z. Xiao, Improving the k – ω – γ – A_r transition model by the field inversion and machine learning framework, *Phys. Fluids* **32**, 064101 (2020).
- [33] E. Parish and K. Duraisamy, A paradigm for data-driven predictive modeling using field inversion and machine learning, *J. Comput. Phys.* **305**, 758 (2016).
- [34] C. Yan, H. Li, Y. Zhang, and H. Chen, Data-driven turbulence modeling in separated flows considering physical mechanism analysis, *Int. J. Heat Fluid Flow* **96**, 109004 (2022).
- [35] Y. Bin, L. Chen, G. Huang, and X. I. A. Yang, Progressive, extrapolative machine learning for near-wall turbulence modeling, *Phys. Rev. Fluids* **7**, 084610 (2022).
- [36] Y. Bin, G. Huang, and X. I. A. Yang, Data-enabled recalibration of the Spalart–Allmaras model, *AIAA J.* **61**, 1 (2023).
- [37] Y. Bin, X. Hu, J. Li, S. Grauer, and X. I. A. Yang, Constrained re-calibration of two-equation Reynolds-averaged Navier–Stokes models, *Theor. Appl. Mech. Lett.* **14**, 100503 (2024).

- [38] X.-L. Zhang, H. Xiao, X. Luo, and G. He, Ensemble Kalman method for learning turbulence models from indirect observation data, *J. Fluid Mech.* **949**, A26 (2022).
- [39] G. Evensen, The Ensemble Kalman Filter theoretical formulation and practical implementation, *Ocean Dynamics* **53**, 343 (2003).
- [40] H. Kato and S. Obayashi, Integration of CFD and wind tunnel by data assimilation, *J. Fluid Sci. Technol.* **6**, 717 (2011).
- [41] D. Driver and L. Seegmiller, Features of a reattaching turbulent shear layer in divergent channel flow, *AIAA J.* **23**, 163 (1985).
- [42] A. Seifert and L. Pack, Active flow separation control on wall-mounted hump at high Reynolds numbers, *AIAA J.* **40**, 1363 (2002).
- [43] M. Barri, G. El Khoury, H. Andersson, and B. Pettersen, DNS of backward-facing step flow with fully turbulent inflow, *Int. J. Numer. Methods Fluids* **64**, 777 (2010).
- [44] H. C. Godinez and J. D. Moulton, An efficient matrix-free algorithm for the ensemble Kalman filter, *Comput. Geosci.* **16**, 565 (2012).
- [45] Turbulence Modeling Resource-2D Backward Facing Step, NASA, https://turbmodels.larc.nasa.gov/backstep_val_sa.html (Accessed: 2023-06-07).
- [46] Turbulence Modeling Resource-2D Wall Mounted Hump, NASA, https://turbmodels.larc.nasa.gov/nasahump_val.html (Accessed: 2023-06-07).
- [47] T. Brooks, M. Marcolini, and D. Pope, Airfoil trailing-edge flow measurements, *AIAA J.* **24**, 1245 (1986).
- [48] A. Di Mascio, R. Broglia, and R. Muscari, Prediction of hydrodynamic coefficients of ship hulls by high-order Godunov-type methods, *J. Mar. Sci. Technol.* **14**, 19 (2009).
- [49] J. Bridges and M. Wernet, Establishing consensus turbulence statistics for hot subsonic jets, in *16th AIAA/CEAS aeroacoustics conference, Stockholm, Sweden* (AIAA, Reston, VA, 2010), p. 3751.
- [50] J. Bridges and M. Wernet, The NASA subsonic jet particle image velocimetry (PIV) dataset, *Tech. Rep.* (2011).